Two-Phase Modeling of Hot Tearing in Aluminum Alloys: Applications of a Semicoupled Method

V. MATHIER, S. VERNÈDE, P. JARRY, and M. RAPPAZ

Hot tearing formation in both a classical tensile test and during direct chill (DC) casting of aluminum alloys has been modeled using a semicoupled, two-phase approach. Following a thermal calculation, the deformation of the mushy solid is computed using a compressive rheological model that neglects the pressure of the intergranular liquid. The nonzero expansion/compression of the solid and the solidification shrinkage are then introduced as source terms for the calculation of the pressure drop and pore formation in the liquid phase. A comparison between the simulation results and experimental data permits a detailed understanding of the specific conditions under which hot tears form under given conditions. It is shown that the failure modes can be quite different for these two experiments and that, as a consequence, the appropriate hot tearing criterion may differ. It is foreseen that a fully predictive theoretical tool could be obtained by coupling such a model with a granular approach. These two techniques do, indeed, permit coverage of the range of the length scales and the physical phenomena involved in hot tearing.

DOI: 10.1007/s11661-008-9772-2

I. INTRODUCTION

HOT tearing is a severe defect that occurs in solidification processes. Tears form in the mushy zone due to the interplay between two main mechanisms: deformation of the partially coherent solid and lack of interdendritic liquid feeding.[1–4] This phenomenon has been studied for several decades, from both theoretical and experimental standpoints. Classical hot tearing tests, which consist of inducing strains in a mushy alloy,[5,6] have been reviewed in Reference 1. From the modeling point of view, continuum-scale approaches have been developed, in order to predict the occurrence of hot tears at least semiquantitatively.[7,8]

In order to obtain a quantitative numerical tool for the prediction of hot tearing, several important contributions have been reported. First, a description of the mechanical behavior of mushy alloys is necessary. In this area, a major contribution for aluminum alloys has been proposed recently by Ludwig *et al*.[9] This work has provided crucial information for the relevant prediction of the amount of strain and the magnitude of the strain rate experienced by the material in the mushy state. Second, the problem of feeding the mushy zone by the intergranular liquid has been addressed in the porosity model of Pequet *et al*.,[10] using a refined mesh locally. Third, the probability of finding a hot tear in a casting can be assessed by defining a suitable hot tearing criterion. Various criteria have been proposed in the literature and are reviewed in Reference 1. These criteria can be based on a critical quantity such as the stress,[11] the strain,[12] or the strain rate.[4] Lately, a granular approach, in which the mushy zone is considered as a population of discrete solid grains surrounded by the liquid phase, has been explored.[13,14] Such models bring complementary information to the standard mixture approach used in continuum-scale modeling. However, they cover length scales that are too small for them to be applicable for the entire process scale.

In order to model hot tearing using a two-phase average approach, it is necessary to solve three problems: energy conservation, momentum conservation, and liquid flow in the mushy zone (possibly coupled with the nucleation and growth of microporosity). Moreover, they must be addressed at the scale of the entire process. A method for doing this was proposed recently by M'Hamdi *et al*.;[8] the resulting software is known as TearSim (SINTEF Materials Technology, Oslo, Norway). These authors proposed a fully coupled resolution scheme in which both the interdendritic feeding and the deformation of the casting are calculated simultaneously. This approach was used to model both laboratory-scale[15] and industrial[16] experiments. More recently, a semicoupled version of this problem has been proposed by the present authors:[17,18] this approach neglects the pressure in the liquid, the deformation of the solid is first calculated. From this, the volumetric (swelling) component of the strain tensor is known and the pressure drop in the liquid is then computed separately. Considering the large difference between the stresses in the solid and the pressure in the

---

V. MATHIER, Software Developer, is with Calcom-ESI SA, Parc Scientifique, CH-1015, Lausanne, Switzerland. M. RAPPAZ, Professor, Computational Materials Laboratory, Institute of Materials Science, School of Engineering, is with the Ecole Polytechnique Fédérale de Lausanne, CH-1015 Lausanne, Switzerland. Contact e-mail: vincent.mathier@esi-group.com S. VERNÈDE and P. JARRY, Ingénieurs expert de recherché, are with the Alcan CRV, FR-38341 Voreppe, France.

Manuscript submitted July 22, 2008.

liquid, this approach corresponds to only a slight loss in accuracy and offers the great advantage of permitting implementation *via* commercial software. In the present article, this semicoupled modeling approach is used to discuss in detail experimental results that are available for a laboratory-scale hot tearing test and an industrial direct-chill (DC) cast-aluminum billet.

II. NUMERICAL MODEL

In order to address problems in which a mushy alloy experiences strain, a semicoupled approach was selected because of its flexibility. Details about this method can be found in References 17 and 18; a summary can be found in References 19 and 20. Only a very brief reminder about this model is thus given here. In this model, the thermal field evolution in the casting is calculated using an appropriate finite element package (CalcoSOFT 3D*). The volume fraction of the solid field can be deduced from the solidification path $g_s^0(T)$ (see Table I for the list of symbols), which is input by the user. This solidification path can be calculated using a microsegregation model or can be measured from thermal analyses.

Once a good description of the thermal field is available, the problem of mass and momentum conservation can be addressed. In general, the two-phase momentum conservation equation can be written as[8]

$$\nabla\cdot\boldsymbol{\sigma}_{\text{eff}} + \bar{\rho}\mathbf{g} = \nabla p_l \qquad [1]$$

where $\bar{\rho} = g_s\rho_s + g_l\rho_l$ is the two-phase averaged density, p_l is the pressure in the liquid phase, and $\mathbf{g}$ is the gravity vector. The effective stress $\boldsymbol{\sigma}_{\text{eff}} = \boldsymbol{\sigma} + p_l\mathbf{I}$ is defined from the total (measured) stress $\boldsymbol{\sigma}$. The present approach is applicable to cases in which the liquid pressure and its variation remain small (compared to the stress and its gradient), so that it is reasonable to neglect its effect on the mechanical problem. The usual expression of momentum conservation is thus solved to obtain the strain and strain rate fields in the sample:[20]

$$\nabla\cdot\boldsymbol{\sigma} + \bar{\rho}\mathbf{g} = 0 \qquad [2]$$

The resolution of this problem is carried out using the thermal field (calculated before the mechanical

Table I. List of Symbols

Symbol	Meaning	Unit
α	rate of evolution of cohesion at low strain	—
A_2, A_3	softening functions	—
C	internal variable describing the cohesion of the mushy alloy	—
C^*	saturation value of the cohesion	—
$\dot{\boldsymbol{\varepsilon}}^{vp}$	viscoplastic strain rate tensor	s^{-1}
$\dot{\varepsilon}_0$	thermally activated coefficient	s^{-1}
$\dot{\varepsilon}_{cr}$	creep (constant volume) characteristic strain rate	s^{-1}
$\dot{\varepsilon}_{sw}$	swelling (volumetric) characteristic strain rate	s^{-1}
ϕ	grain size	m
$\mathbf{g}$	gravity vector	—
g_s	solid fraction (g_s^0 is the solid fraction under zero strain)	—
g_s^{coh}	coherency point (above this solid fraction, strains are transmitted to the mushy alloy)	—
g_s^{coal}	coalescence point (above this solid fraction, the alloy behaves like a continuous solid)	—
$\mathbf{I}$	unit tensor	—
κ	characteristic strength in Ludwik's model	Pa
K	permeability of the solid skeleton	m^2
l	subscript indicating the liquid phase	—
λ	strain rate sensitivity in Ludwik's model	—
μ	viscosity of the liquid phase	Pa s
η	strain sensitivity in Ludwik's model	—
n	exponent of the power law creep	—
P_s	pressure in the solid phase (first invariant of the stress tensor)	Pa
p_l	pressure in the liquid phase	Pa
ρ_l	density of the liquid phase	kg m^{-3}
$\bar{\rho}$	average density of the mixture of phases	kg m^{-3}
T_ε	temperature limit for strain accumulation	°C
T	temperature	°C
σ_M	von Mises stress (second invariant of the stress tensor)	Pa
$\boldsymbol{\sigma}$	total stress	Pa
$\boldsymbol{\sigma}_{\text{eff}}$	effective stress	Pa
s	subscript indicating the solid phase	—
s_0	characteristic stress resistance of the solid phase	Pa
$\mathbf{v}_s$	solid velocity	m s^{-1}

---

*CalcoSOFT 3D is a trademark of ESI-Group, Paris, France.

simulation) as input. The rheology of the material is described using the model of Ludwig *et al.*,[9] which has been implemented in Abaqus**. Assuming that the viscoplastic strain rate is a function of both the deviatoric stress $\mathbf{S}$ and hydrostatic pressure P_s (*i.e.*, the mushy solid is compressible), this model takes the following form for the coherent mushy zone (*i.e.*, for $g_s > g_s^{\mathrm{coh}}$):

$$\dot{\boldsymbol{\varepsilon}}^{vp} = \frac{\dot{\varepsilon}_0}{(Cs_0)^n}\left(A_2 P_s^2 + A_3 \sigma_M^2\right)^{\frac{n-1}{2}}\left(-\frac{A_2}{3}P_s\mathbf{I} + \frac{3}{2}A_3\mathbf{S}\right) = \dot{\varepsilon}_{sw}\mathbf{I} + \frac{3}{2}\frac{\dot{\varepsilon}_{cr}}{\sigma_M}\mathbf{S} \qquad [3]$$

where $\dot{\boldsymbol{\varepsilon}}^{vp} = \frac{1}{2}\left(\nabla\mathbf{v}_s + \nabla\mathbf{v}_s^T\right)$ is the viscoplastic strain rate tensor, $\dot{\varepsilon}_0 = A\exp\left(-\frac{Q}{\mathrm{R}T}\right)$ is a thermally activated coefficient, $\dot{\varepsilon}_{sw}$ and $\dot{\varepsilon}_{cr}$ are the volumetric (swelling in Abaqus) and deviatoric (creep in Abaqus) equivalent strain rates, respectively, $P_s = -\frac{1}{3}\mathrm{tr}(\boldsymbol{\sigma})$ is the pressure in the solid, $\mathbf{S} = \boldsymbol{\sigma} + P_s\mathbf{I}$ is the deviatoric stress tensor, and σ_M its second invariant ($\sigma_M^2 = \frac{3}{2}\mathbf{S}:\mathbf{S}$). C is a cohesion internal variable, which varies from 0 (freely floating solid grains in liquid) to 1 (dense solid or fully coalesced granular skeleton). The details about the development and meaning of this relation are given in Reference 9. It should be remembered that the mushy zone is a compressible medium (solid grains can be brought together or pulled apart, *i.e.*, strain can change the specific volume of the mushy alloy); this feature is captured by this equation. This is an important aspect of that model, from the point of view of hot tearing studies.

The model is completed by an evolution equation for the internal variable C:[9]

$$\frac{dC}{dt} = \alpha\left(1 - \frac{C}{C^*}\right)\sqrt{\frac{2}{3}\dot{\boldsymbol{\varepsilon}}^{vp}:\dot{\boldsymbol{\varepsilon}}^{vp}} \qquad [4]$$

The evolution of this internal variable takes into account the fact that the mushy alloy behavior is dependent upon the stress state it experiences (the value of C^* depends upon the stress state). The effect of the coalescence of the grains at a high solid fraction is also introduced above a critical fraction g_s^{coal} of typically 96 pct in the expression of coherency C.[9] The materials parameters that appear in this model were determined by experimental identification.[9,21,22]

In the case of the fully solid material ($g_s = 1, C = 1$), this model takes a more classical form:

$$\dot{\boldsymbol{\varepsilon}}^{vp} = \frac{3}{2}\frac{\dot{\varepsilon}_{cr}}{\sigma_M}\mathbf{S} \quad \text{with } \dot{\varepsilon}_{cr} = \frac{\dot{\varepsilon}_0}{s_0^n}\sigma_M^n \qquad [5]$$

This expression is suitable for describing the mechanical behavior of aluminum alloys typically above 400 °C.[22] At lower temperatures, strain-hardening effects become significant and it is thus necessary to introduce a generalized Ludwik model:[22–24]

$$\sigma_M = \kappa(T)\varepsilon_{cr}^{\eta(T)}\left(\frac{\dot{\varepsilon}_{cr}}{\dot{\varepsilon}_u}\right)^{\lambda(T)}$$

$$\text{with } \varepsilon_{cr} = \int_{t(T<T_\varepsilon)}^{t}\dot{\varepsilon}_{cr}dt \text{ and } \dot{\varepsilon}_u = 1\ \mathrm{s}^{-1} \qquad [6]$$

where the creep strain ε_{cr} can only accumulate below T_ε (the temperature below which strain hardening becomes significant). The strain sensitivity η and strain-rate sensitivity λ are temperature-dependent functions (typically $\eta(T)$ is low at high temperature and high at low temperature, while it is the opposite for $\lambda(T)$).

Having solved the mechanical problem, the velocity field in the solid, $\mathbf{v}_s$, is known. Please note that $\nabla\cdot\mathbf{v}_s = \dot{\varepsilon}_{sw} \neq 0$ (mushy zone compressibility). This term becomes a source term in the mass conservation equation. The latter is combined with Darcy's law for the calculation of the pressure p_l in the liquid, to give[8]

$$\frac{\partial\bar{\rho}}{\partial t} + \nabla\cdot(\bar{\rho}\mathbf{v}_s) - \nabla\left(\frac{\rho_l K}{\mu}(\nabla p_l - \rho_l\mathbf{g})\right) = 0 \qquad [7]$$

where $\mu(T)$ is the viscosity of the liquid phase and $K = \frac{(1-g_s)^3}{g_s^2}\frac{\phi^2}{180}$ is the permeability of the solid skeleton. This quantity depends on the grain size ϕ for equiaxed microstructures. Equation [7] is solved using the ProCAST† advanced porosity module, after implementation of the additional term $\nabla\cdot\mathbf{v}_s = \dot{\varepsilon}_{sw}$.[10] The formation of porosity due to the presence of hydrogen dissolved in the alloy can also be predicted using the full model described in Reference 10. As a summary, the flow chart of the model is presented in Figure 1.

Finally, please note that the solid fraction takes into account the effect of strain in both the mechanical and porosity calculations. For these cases, the solidification path $g_s^0(T)$, which is provided as input and is used directly in the heat flow simulation, is corrected according to

$$g_s^\varepsilon = g_s^0(T)\left(1 - \int_t \mathrm{tr}(\dot{\boldsymbol{\varepsilon}}^{vp})dt\right) \qquad [8]$$

where $g_s^\varepsilon(T)$ is the volume fraction of the solid under deformation conditions and $g_s^0(T)$ is the usual solidification path without applied strain. (In the discussion

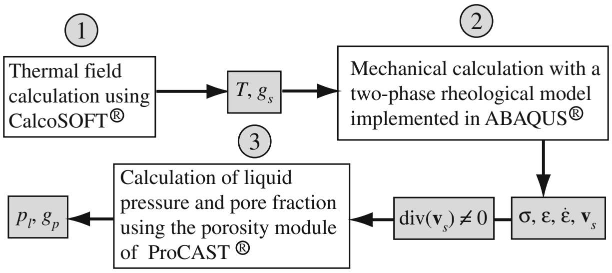

Fig. 1—Flow chart of the semicoupled approach.

**Abaqus is a trademark of Abaqus Inc., Pawtucket, RI.

†ProCAST is a trademark of ESI-GROUP, Paris, France.

that follows, we use the notation g_s to denote $g_s^{\varepsilon}(T)$; $g_s^0(T)$ will be used only when the thermal solid fraction is specifically referred to.)

III. RIG-TEST APPLICATION

A. *Experimental Data*

For a first application of the present modeling approach, we consider tensile test data for an Al-2 wt pct Cu alloy; these data were obtained using the rig test of Magnin *et al.*[12] Let us first briefly recall the description of this test. As illustrated in Figure 2, a dog-bone-shaped mold is opened at the top and connected to a filling system at the bottom. One end of the mold acts as a fixed jaw, while the other is fixed to a tensile test machine. At the beginning of the test, the top of the mold is closed using a steel chill. Liquid alloy is poured through the filling system and the mold is filled from the bottom. During the first 10 seconds, the alloy in contact with the steel chill solidifies. The chill is then removed. From this time, heat is mostly extracted through the jaws; this leads to a hot spot at the center of the specimen (this effect is enhanced by the presence of liquid alloy in the filling system). During casting, the temperature is recorded by four thermocouples positioned at various locations in the vicinity of this hot spot. When the temperature reaches a value corresponding to the desired solid fraction, the tensile test is started by moving the mobile jaw at a constant displacement rate $\dot{u}_z$, which takes the following values: 2.5, 10, or 40 mm min^{-1}. Please note that the cooling conditions are such that, when the tensile tests are performed, the isotherms are roughly perpendicular to the direction of applied displacement (*i.e.*, axial direction of the specimen).

B. *Model Parameters*

For symmetry reasons, only a quarter of the casting was considered in the simulation. The geometry of the filling system is not modeled very accurately, but this did not have any significant effect on the results. The various model conditions are summarized in Figure 3 and Table II. For the sake of simplicity, the heat transfer at boundaries that are not symmetry elements is modeled using a convective heat-transfer condition, in which the external temperature is 20 °C. Most of the heat is extracted through the jaw, so that their temperature increases during the test, leading to a decrease in the cooling intensity. This effect is taken into account by using a heat-transfer coefficient that depends on the surface temperature of the alloy, where it is in contact with the jaws (Figure 4). The solidification path $g_s^0(T)$ that was used in the computations is shown in Figure 5, together with the lever rule and the Scheil–Gulliver approximations corresponding to this alloy. The solidification path was obtained from the thermal measurements and was slightly modified for very high solid fractions, in order to account for the delayed completion of solidification due to coalescence, as illustrated in Reference 14.

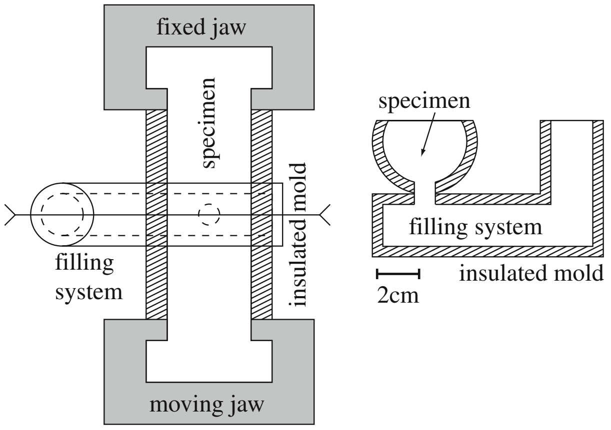

(a) top view **(b)** vertical cross section

Fig. 2—Schematic mold design for the rig test.

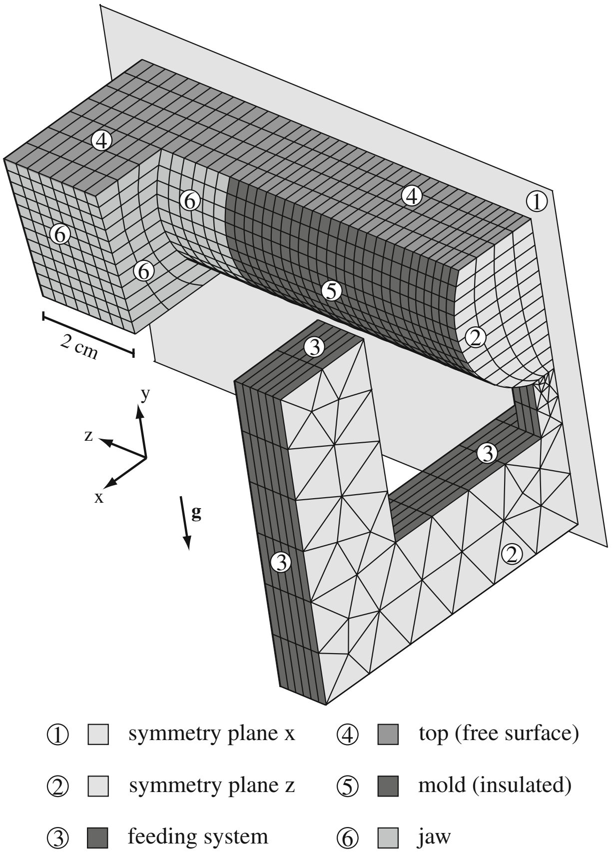

Fig. 3—Thermal boundary conditions used to model the rig test.

The mechanical model is set up using the same mesh without taking the filling system into account. The modeling conditions are summarized in Table III. During the tensile test, the nodes that are in contact with the jaws move at a velocity corresponding to the applied displacement rate of the experiment (the symmetry effect being taken into account), while other degrees of liberty are free (zero force in all directions). This allows prediction of the reaction force, which should be equivalent to the force measured during the actual tensile test.

Table II. Summary of Parameters Involved in Thermal Simulation of Rig Test

Thermal Boundary Condition as Defined in Fig. 3	h in $\mathrm{Wm^{-1}\,K^{-1}}$ ($T_{\mathrm{ext}} = 20$ °C)
1: Planar symmetry	zero heat flux ($h_1 = 0$)
2: Planar symmetry	zero heat flux ($h_2 = 0$)
3: Filling system	$h_3 = 5$, $T_{\mathrm{ext},3} = 20$
4: Top surface	first 10 s (chill contact): $h_4 = 2000$ after chill removal: $h_4 = 10$
5: Gage length of the sample	$h_5 = 5$
6: Jaws of the tensile test machine	h_6 as in Figure 4
Properties of the Al-2 wt pct Cu sample	
Thermal conductivity	$\kappa = 200\ \mathrm{Wm^{-1}\,K^{-1}}$
Heat capacity	$\rho C_p = 2.9 \times 10^6\ \mathrm{Jm^{-3}\,K^{-1}}$
Latent heat	$\rho L = 8 \times 10^8\ \mathrm{Jm^{-3}}$

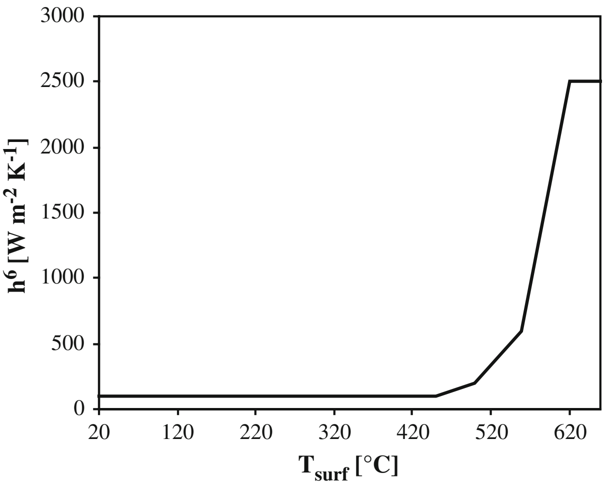

Fig. 4—Equivalent convective heat-transfer coefficient used to model cooling by the jaws in the rig test.

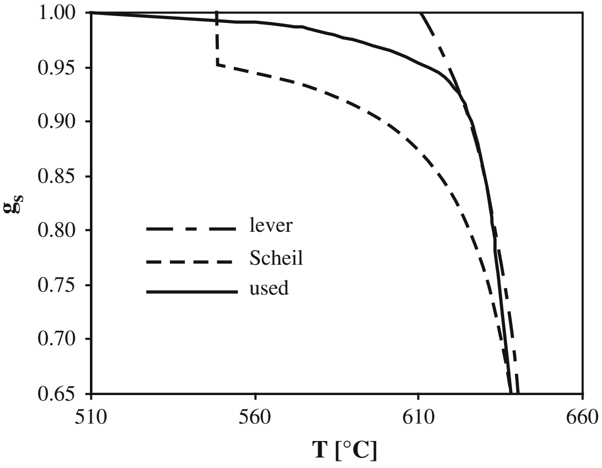

Fig. 5—Solid fraction plotted against temperature relation used for the Al-2 wt pct Cu alloy.

The low value of the apparent Young's modulus is due to the fact that it actually corresponds to an effective value. The compliance of the tensile test machine is, indeed, included in this Young's modulus, the value of which was obtained after calibration of the tensile experiment with a fully solidified sample at room temperature. Thermal contraction of the sample was found to be negligible when compared to the strain rate applied by the tensile test machine and is thus neglected (note that before the tensile test, free contraction of the sample is allowed). The rheology of the alloy in the mushy state was described using the parameters from Reference 9 (partially recalled in Table IV).

The low-temperature properties are described using a generalized Ludwik model (Eq. [6]), with the parameters from Reference 24 summarized in Table V. The parameters κ, η, and λ are temperature dependent (coefficients c_i^{κ}, c_i^{η}, and c_i^{λ}, respectively). This constitutive law is used below 520 °C (while strain hardening becomes significant below 423 °C), which ensures that the alloy rheological properties are continuous across the entire temperature range.

Finally, the porosity calculation was conducted using an estimate of the amount of hydrogen dissolved in the melt $[\mathrm{H}]_0 = 0.3\ \mathrm{cc_{STP}}/100$ g. A constant grain size $\phi = 100\ \mu$m was used, together with standard parameters given elsewhere.[10]

Both the thermal and porosity calculations were conducted on an Intel Xeon[‡] processor (2 GHz). The temperature field was simulated using elements 1.7 mm in size and time-steps of 2 seconds. The CPU time was 1 minute, corresponding to 400 seconds of physical time. The pore fraction and liquid pressure were calculated using cells 1 mm in size and a time-step of 0.1 second. The CPU time was 1.5 hours. The mechanical problem was solved on an Intel Itanium 2[§] processor (1.6 GHz) with elements 1.7 mm in size and an average time-step of typically 10^{-4} seconds (automatic time incrementation with the Abaqus parameter CETOL = 10^{-6}[17]). To simulate 10 seconds of an actual tensile test, the CPU time was 6 hours. All these numerical parameters

---

[‡] Intel Xeon is a trademark of Intel Corporation, Santa Clara, CA.

[§] Intel Itanium is a trademark of Intel Corporation, Santa Clara, CA.

Table III. Summary of Parameters Involved in Mechanical Calculation

Mechanical boundary condition as defined in Fig. 3	Value
1: Planar symmetry	fixed in the normal direction ($u_x = 0$) and free to move in other directions ($F_y = F_z = 0$)
2: Planar symmetry	fixed in the normal direction ($u_z = 0$) and free to move in other directions ($F_x = F_y = 0$)
3: Free face	$F_x = F_y = F_z = 0$
4: Free face	$F_x = F_y = F_z = 0$
5: Free face	$F_x = F_y = F_z = 0$
6: jaws of the tensile test machine	$\dot{u}_z$ prescribed ($F_x = F_y = 0$), equivalent to experimental values : 2.5, 10 or 40 mm min^{-1}
Properties of the Al-2 wt pct Cu sample	
Young's modulus	$E = 2.6$ GPa at 20 °C; $E = 2$ GPa at 540 °C and drops down to $E = 0.1$ GPa at 620 °C
Poisson's ratio	$v = 0.33$

Table IV. Parameters Describing Rheology of Mushy Al-2 Weight Percent Cu Alloy

s_0 (MPa)	A (s^{-1})	Q (kJmol^{-1})	n
4.77	9×10^5	154	3.8

were determined after a convergence study was performed for idealized conditions, to ensure that the simulated solution would not change significantly if smaller elements and shorter time-steps were used.

C. *Results and Discussion*

The temperatures measured in the region of the hot spot were compared successfully to the values predicted by the model, as illustrated in Figure 6. In this figure, the position of the thermocouples is displayed; also displayed is the comparison between typical experimental (thin gray lines) and simulated (thick black lines) temperatures at these locations. It was found that the cooling rate in the mushy alloy during the tensile test has a typical value of $\dot{T} = -2\ \text{Ks}^{-1}$. Using the simulation results, the thermal gradients in the sample could be measured accurately, as could the average temperature value, T_{center}, in the central section of the specimen. The thermal gradient in both the longitudinal (G_z, due to cooling from the jaws of the tensile test machine) and vertical (G_y, due to the presence of hot liquid in the filling system at the bottom of the hot spot) are plotted against T_{center} in Figure 7. As can be seen, both components of the gradient vary between 0.7 and 1.7 K/mm, depending on the temperature. The longitudinal gradient G_z is desired, in order to create a hot spot at the center of the specimen in a direction parallel to the stress direction. On the other hand, the G_y component, which is unavoidable in this setup, introduces a temperature difference in the plane in which strains will be concentrated and disrupts somewhat the interpretation of the results.

The results of the mechanical simulation indicate that the stress (*i.e.*, reaction force) depends on the temperature and the applied displacement rate in a fashion similar to that observed in the actual experiments. A sample comparison between the simulated and measured reaction force is illustrated in Figure 8. The maximum stress that is reached is much higher in the simulation than in the experiment, because no failure model is included in the numerical computation (*i.e.*, we do not have a hot tearing criterion at this point), while

Table V. Rheological Parameters for Al-2 Weight Percent Cu Alloy at Moderate Temperature (Equation [6]) (*T* is the Temperature Expressed in Kelvin)

$\kappa = c_1^{\kappa}\left(1 - c_2^{\kappa}\tanh\left(\frac{T - c_4^{\kappa}}{c_3^{\kappa}}\right)\right)$				
c_1^{κ}	c_2^{κ}	c_3^{κ}		c_4^{κ}
210 MPa	0.75	132		540
$\eta = c_1^{\eta}\left(1 - c_2^{\eta}\tanh\left(\frac{T - c_4^{\eta}}{c_3^{\eta}}\right)\right)$				
c_1^{η}	c_2^{η}	c_3^{η}		c_4^{η}
0.155	1	135		500
$\lambda = c_1^{\lambda} + c_2^{\lambda}T + c_3^{\lambda}T^2 + c_4^{\lambda}T^3 + c_5^{\lambda}T^4$				
c_1^{λ}	c_2^{λ}	c_3^{λ}	c_4^{λ}	c_5^{λ}
-5.17×10^{-5}	2.69×10^{-4}	-2.56×10^{-6}	6.78×10^{-9}	-4.37×10^{-12}

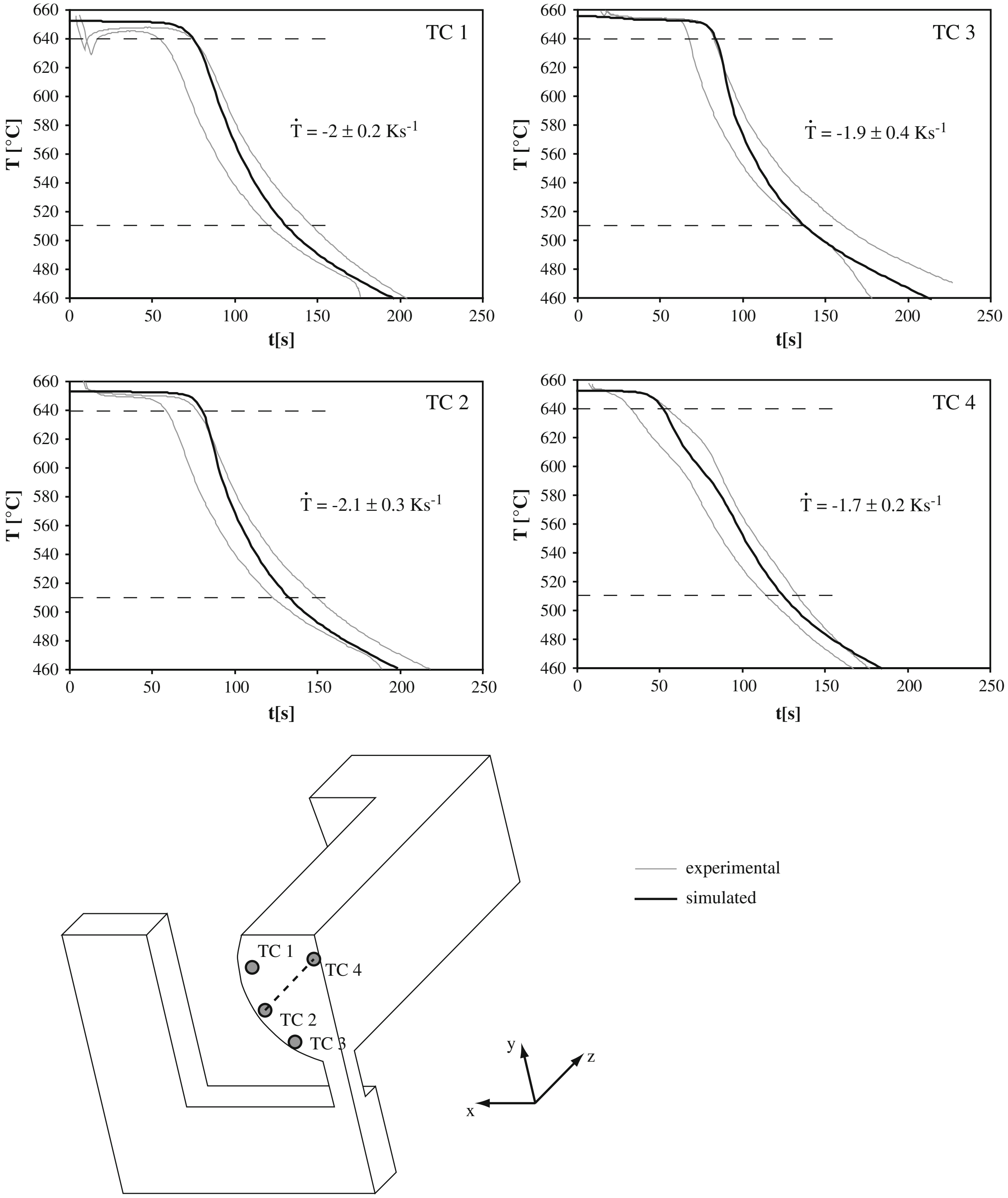

Fig. 6—Position of thermocouples in the sample and comparison, between simulated and measured temperatures at these locations.

tearing (failure) actually occurs in the experiment. The rate of increase in the stress in the mushy alloy before fracture is, in fact, the most interesting quantity involved in predicting tearing. From this point of view, an acceptable agreement was found, because the difference between the simulation and the experiment is on the order of the experimental uncertainty (this uncertainty is suggested by having two different experimental results for the same conditions). These arguments lead to the conclusion that the present model is able to predict how strain is distributed in the sample in a satisfactory way. Please note that only strain-related quantities will be used for further analysis of the results.

The present test is well suited to studying the ductility of the mushy alloy. As reported by Magnin *et al.*,[12] the ductility-*vs*-temperature plot is typically a U-shaped curve. This fact is illustrated in Figure 9 (left), which displays the displacement at failure as a function of the temperature in the hot spot (evaluated when tearing actually occurs). At high temperature, the mushy alloy is very ductile, due to the possibility of the rearrangement of grains and easy liquid feeding. At low temperature, the alloy is fully coalesced and exhibits the high ductility that is characteristic of a fully solid material at high temperature (please note that, at the lowest test temperatures, fracture did not occur and failure is taken to correspond to yielding). In the intermediate temperature range, which corresponds to solid fractions at which hot tearing is expected to occur, there exists a minimum ductility. Such results can be obtained readily from the experimental data alone: the ductility is then estimated from the measured overall displacement at failure of the specimen (divided by the gage length). However, the strain is inhomogeneous along the *z-axis* of this specimen, due to the longitudinal gradient G_z. Simulation results are thus very useful, because they permit the estimation of the actual value of strain at failure at the location at which the tear is actually found.

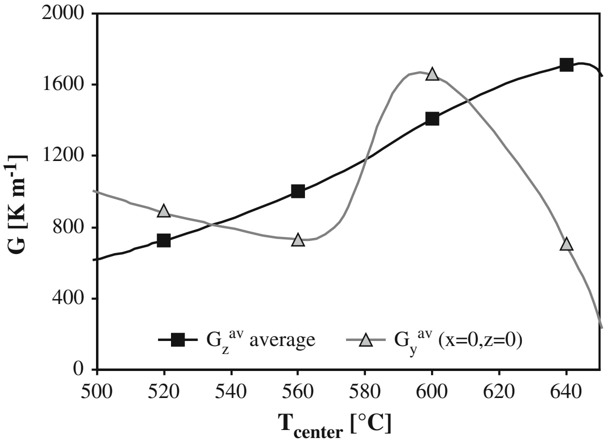

Fig. 7—Longitudinal and vertical thermal gradient in the Al-2 wt pct Cu tensile sample as a function of the average temperature T_{center} in the central cross section of the specimen.

By using the present numerical model, it is possible to obtain directly (from the experimental time to failure) and, with enhanced accuracy, the value of the failure strain at which tearing occurs (*i.e.*, in the central section). This quantity can be plotted as a function of the corresponding temperature in the mushy alloy. Such a result is displayed in Figure 9 (right). There are two important features to notice in these results. First, the ductility of the alloy seems to depend only weakly upon the applied strain rate. Second, this curve indeed exhibits a U shape, but the increase in ductility at low temperature is not as marked, as suggested by the experimental results alone. This is due to the inhomogeneous strain field, as is explained later.

Using the simulated strain rate at failure, it is possible to estimate how the strain is distributed in the sample at the time of failure. For that purpose, one defines a dimensionless number, noted τ_{fail}, which is the ratio of the applied displacement rate $\dot{u}_z$ to the strain rate $\dot{\varepsilon}_{zz,\text{fail}}$ in the center of the specimen at failure, multiplied by the length l_{sample} of the sample

$$\tau_{\text{fail}} = \frac{\dot{u}_z}{\dot{\varepsilon}_{zz,\text{fail}} \cdot l_{\text{sample}}} \qquad [9]$$

For a uniformly strained specimen, $\tau_{\text{fail}} = 1$; it is smaller than unity, however, when strains are localized at the center of the specimen. Using the simulated strain rate at failure and Eq. [9], to compute τ_{fail}, the result shown in Figure 10 is obtained (please note that the

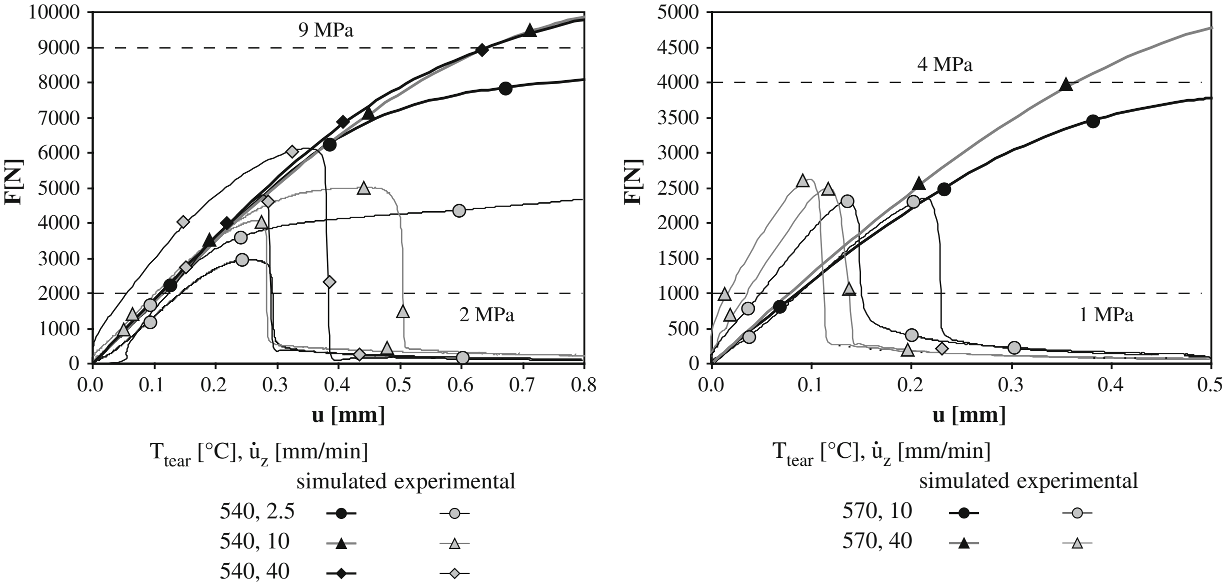

Fig. 8—Comparison between experimental and simulated reaction force. The experimental data were measured using the rig test on an Al-2 wt pct Cu alloy for two temperatures (540 °C and 570 °C) and for different pulling velocities (2.5, 10, and 40 mm/min). Curves with the same line color and symbol shape are to be compared.

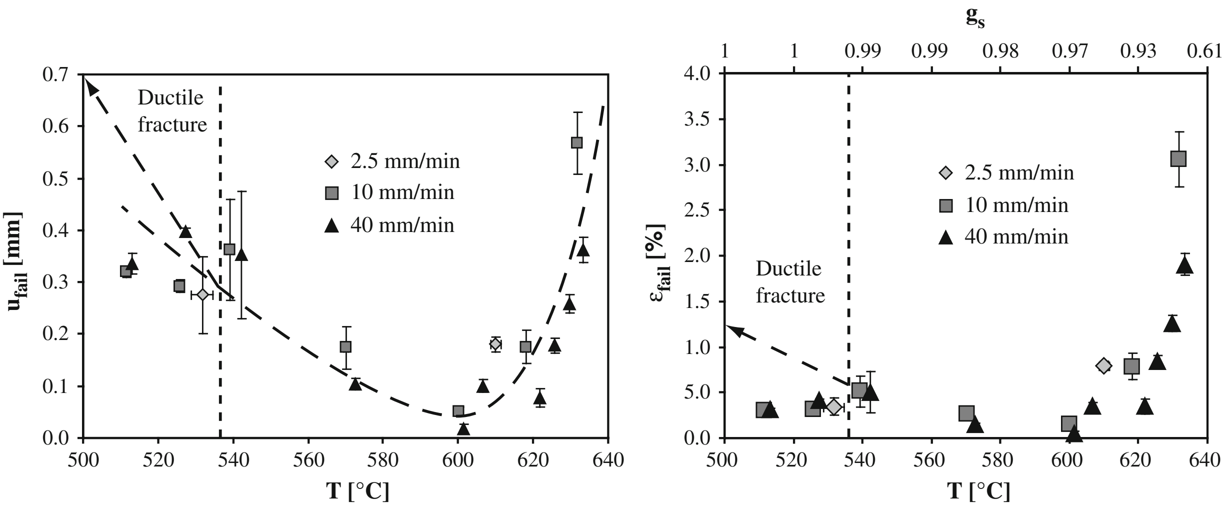

Fig. 9—Left: displacement at failure as a function of temperature in the hot spot when tearing occurs. Right: Strain at failure (ductility) as a function of temperature for the Al-2 wt pct Cu alloy.

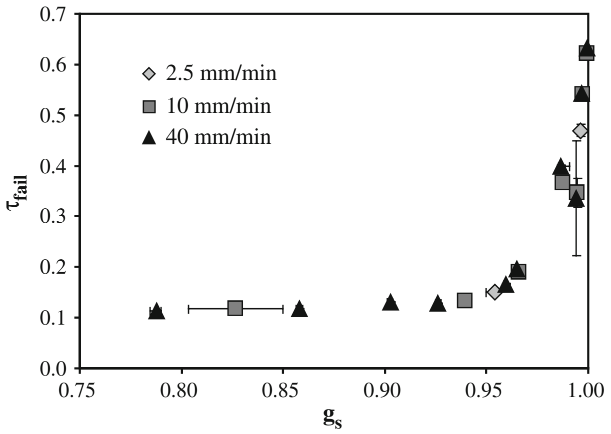

Fig. 10—Strain distribution measure as a function of the solid fraction at the center of the specimen.

temperature scale was converted to a g_s scale). Up to 95 pct of the solid in the hot spot, the strain is distributed across the sample in the same manner: only approximately 10 pct ($\tau_{fail} \approx 0.1$) of the sample length is being effectively deformed in the region of the hot spot. In this regime, the ductility of the alloy may be obtained from the experimental measurements (dividing the displacement at failure by a tenth of the sample length). At higher solid fractions, the strain in the sample gets more and more evenly distributed (the concentration factor τ_{fail} increases rapidly with g_s); this contributes significantly to the apparent ductility (*i.e.*, displacement at failure) of the alloy. As a consequence, the intrinsic ductility of the alloy at high solid fractions can only be evaluated accurately provided an efficient numerical model is available to take into account the strain distribution effects (because the effectively strained length of the sample varies strongly, even for small solid-fraction increments). This is important because only the intrinsic ductility (a material property that should not be dependent upon test geometry, for example) may be used to predict hot tearing in other test setups.

In summary, it appears that the best way to explain hot tearing in the rig test is to consider that there exists a critical amount of strain that the mushy alloy can withstand before breaking. This ductility is strongly dependent upon temperature, is minimum when the solid fraction is close to 95 pct (typical value when hot tears are thought to be formed), and is only weakly dependent upon the strain rate. The value of the ductility can be evaluated only if both experimental and numerical data are available, because it is necessary to make a distinction between the intrinsic properties of the mushy alloys and the strain distribution effects (because the latter are also geometry dependent). Finally, it is worth noting that predictions of the amount of microporosity expected in the sample could be obtained.[18] These results did not provide additional key insights into the failure mechanisms involved in this experiment (the porosity formation pattern is only weakly dependent upon the applied strain).

IV. INDUSTRIAL APPLICATION

A. *Experimental Data*

The present modeling approach was then applied to a more industrially relevant case. The AA5182 billets were DC cast by Commet *et al.*[25] using the casting recipe shown in Figure 11 under industrial conditions. After casting, the detection of the hot tear position (height) along the centerline was performed by ultrasonic (US) measurements. During the start-up phase, hot tearing was avoided up to approximately 1 m of casting. As the casting speed was ramped up from 80 to 140 mm/min, a hot tear formed (point labeled "tear initiation" at approximately 1 m of casting in Figure 11). Afterward, the casting speed was ramped down and the hot tear disappeared once the casting speed was reduced below

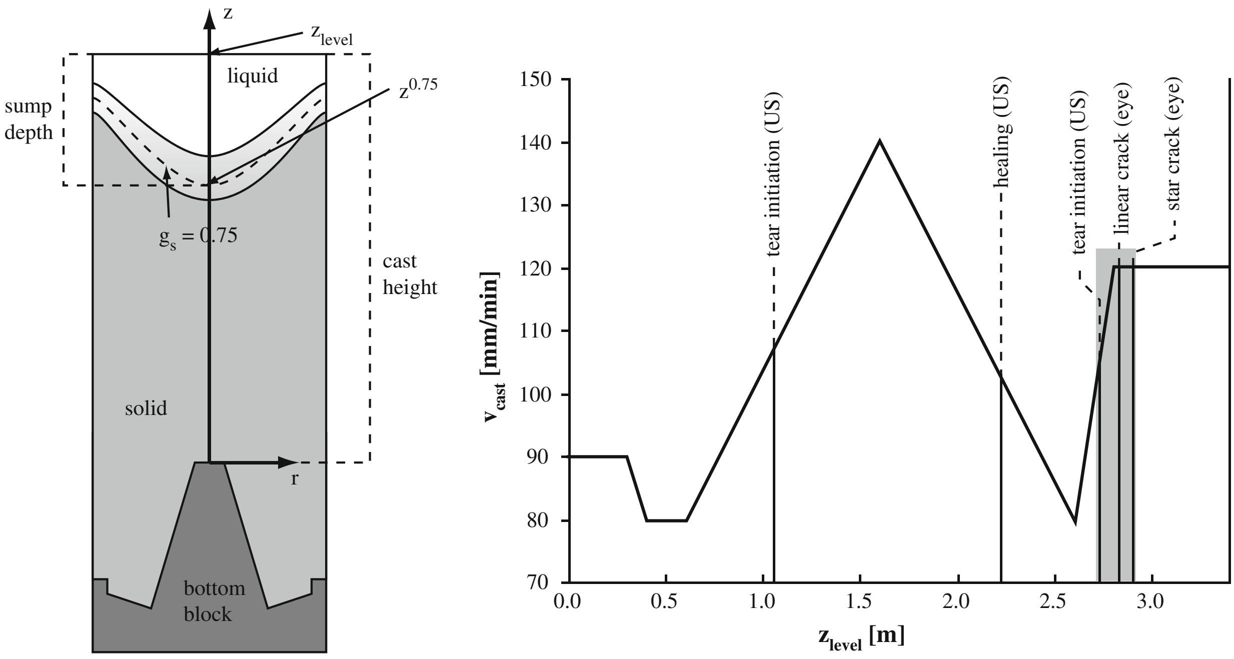

Fig. 11—Geometry of the axisymmetric billet and reference frame used to describe positions in the billet and indication of where the tear is found along the centerline (left). The casting recipe is shown on the right, with the locations at which hot tears were observed (Refs. 25 and 26).

110 mm/s (point labeled "tear healing" at 2.2 m of casting). In a final stage, the casting speed was increased again, so that the hot tear nucleated again at 2.7 m of casting and grew up to the top of the billet.

The development of the hot tear during the last ramping up of the casting speed (region outlined in gray in Figure 11) was further studied by Grasso.[26] The billet was cut into 1-cm-thick slices, to study how the morphology of the tears evolved from an annular porosity distribution to a linear crack and, finally, to a typical three-branch star-shaped crack. Please note that these observations resulted in detection of the onset of the tear slightly later than the US measurements (this is not surprising, because the latter study was performed by techniques involving use of the naked eye). Another piece of experimental information is also available for this billet: the depth of the liquid pool, which was measured during casting by probing the bottom the sump with a rod.

B. *Model Parameters*

Because the DC casting process of the AA5182 billet is axisymmetric, it was treated as such in the present simulation. When looking at the casting in a reference frame attached to the bottom block, the liquid level z_{level} is a function of the time t. Please note that the casting speed v_{cast} is prescribed as a function of the z_{level}, according to

$$\frac{dz_{\text{level}}}{dt} = v_{\text{cast}}(z_{\text{level}}) \qquad [10]$$

The entire final billet was meshed once, for all calculations. Since no boundary condition can be imposed at z_{level}, the following procedure was adopted. The region above z_{level} has its external surface set with an adiabatic boundary condition, whereas its thermal conductivity is fixed to zero. As a consequence, the top liquid surface ($z = z_{\text{level}}$) in the billet will always have a temperature equal to the pouring temperature, which is the same as the initial temperature in the domain. This technique allows for a reasonable treatment of the top liquid surface (*i.e.*, treatment of the hot top apparatus) without having to use an evolving mesh. All the other boundary conditions applied to the billet are summarized in Figure 12 and Table VI. Cooling from the side (2) and bottom (5) of the billet is modeled using a variable convective heat-transfer coefficient and a constant external temperature of 20 °C. The value of the heat-transfer coefficient depends on local conditions (especially for cooling from the side). Just below the liquid surface, the side of the billet is not in contact with the mold (meniscus formed due to bad wetting of the liquid). Below this region, contact is established with the mold down to the point at which an air gap is formed. Below this gap (*i.e.*, on most of the side of the billet), the secondary cooling regime (impingement of the water jet and then the flow of water) is described with a value of h_2 that depends on the surface temperature. The contact with the bottom block is also simulated, using an effective convective heat-transfer coefficient. All these parameters were estimated based on past inverse simulations performed under similar DC casting conditions.[27] The properties of the materials that were used for the AA5182 alloy for the thermal calculation are shown in Table VII.

As far as the mechanical simulation of this process is concerned, the boundary conditions are quite simple, because they are described by the symmetry conditions,

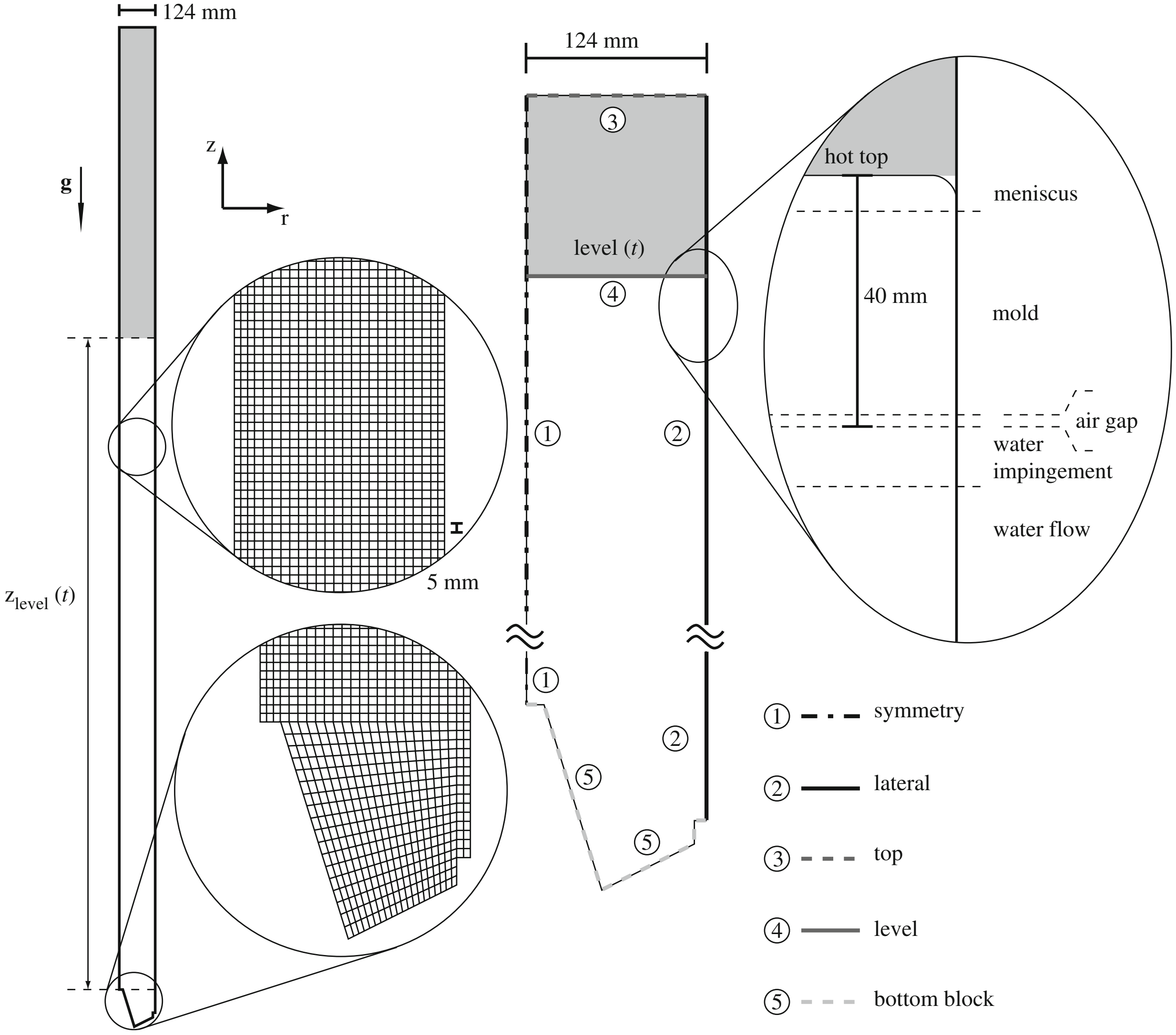

Fig. 12—Summary of the conditions for the simulation of the DC casting process.

Table VI. Summary of Parameters Involved in Thermal Simulation of AA5182 Billet

Thermal Boundary Condition as Defined in Fig. 12	h in $\mathrm{Wm^{-1}\,K^{-1}}$ ($T_{ext} = 20$ °C)
1: Axis of symmetry	zero heat flux ($h_1 = 0$)
2: Cooling on the side	From top to bottom: meniscus: $h_2 = 0$ contact with the mold: $h_2 = 500$ air gap: $h_2 = 100$ secondary cooling: typically, $h_2 = 10{,}000$ for surface temperatures above 350 °C and peak values of $h_2 = 40{,}000$ for a surface temperature of 150 °C
3: Top surface	$h = 0$
4: Top liquid level	imposed temperature 670 °C ($h = 0$ and zero thermal conductivity above)
5: Bottom block	$h_5 = 800$ (except close to the centerline, where $h = 250$)
Properties of the AA5182 billet	
Thermal conductivity	$\kappa = 160\ \mathrm{Wm^{-1}\,K^{-1}}$ (increased to $250\ \mathrm{Wm^{-1}\,K^{-1}}$ in the liquid phase, to simulate the effect of convection)
Heat capacity	$\rho C_p = 3 \times 10^6\ \mathrm{Jm^{-3}\,K^{-1}}$
Latent heat	$\rho L = 9 \times 10^8\ \mathrm{Jm^{-3}}$

Table VII. Summary of Parameters Involved in Mechanical Calculation

Mechanical boundary condition as defined in Fig. 12	Value
1: Axis of symmetry	fixed in the radial direction ($u_r = 0$) and free to move in longitudinal directions ($F_z = 0$)
2: Side	free ($F_r = F_z = 0$)
3: Top surface	free ($F_r = F_z = 0$)
4: Top liquid level	free ($F_r = F_z = 0$)
5: Bottom block	free ($F_r = F_z = 0$) except for the centerline node that is fixed in $z : u_z = 0$
Properties of AA5182 billet	
Young's modulus	$E = 72$ GPa at 20 °C; $E = 41$ GPa at 400 °C and drops down to $E = 0.1$ GPa at 610 °C
Poisson's ratio	$v = 0.33$

Table VIII. Parameters Describing the Rheology of the Mushy Zone AA5182 Alloy

s_0 (MPa)	A (s^{-1})	Q (kJmol^{-1})	n
52	2.67×10^7	125	3.44

while one node (on the centerline and in contact with the bottom block) is fixed. All the other faces are free to move. Please note that, in order to save CPU time, only the elements below z_{level} are activated at each time-step for this calculation. The strains that develop in the solid and mushy alloy are due to differential thermal expansion. Following Stangeland *et al.*,[28] the thermal expansion coefficient was set to $\alpha = 25 \times 10^{-6}\ \text{K}^{-1}$ for $g_s > 0.8$ and 0 for higher temperatures. The rheology of the alloy at high temperature was described using the parameters from Reference 21, which are partially recalled in Table VIII.

The low-temperature properties are described using the generalized Ludwik model, with the parameters from Reference 22 summarized in Table IX. The latter constitutive law is used below 410 °C (while strain hardening becomes significant below 400 °C), which ensures that the alloy rheological properties are continuous across the entire temperature range.

Finally, the porosity calculation was conducted using the amount of hydrogen dissolved in the melt $[\text{H}]_0 = 0.3\ \text{cc}_{\text{STP}}/100$ g, as measured during the casting process. A constant grain size $\phi = 100\ \mu$m was used, together with standard parameters given elsewhere.[10]

Both the thermal and porosity calculations were conducted on an Intel Xeon processor (2 GHz). The temperature field was simulated using elements 5 mm in size and a time-step of 1 second. The CPU time was 4 hours, corresponding to 2000 seconds of physical time. The pore fraction and liquid pressure were calculated using cells 3 mm in size and a time-step of 1 second. The CPU time was 48 hours. The mechanical problem was solved on an Intel Itanium 2 processor (1.6 GHz) with elements 5 mm in size and an average time-step of typically 10^{-3} seconds (automatic time incrementation with the Abaqus parameter CETOL = 5×10^{-5}[17]). To simulate the casting of the entire billet, the CPU time was 566 hours. All these numerical parameters were determined after a convergence study was performed for idealized conditions, to ensure that the simulated solution would not change significantly if smaller elements and shorter time-steps were used.

C. *Results and Discussion*

Because the aim of this section is to study hot tearing formation along the centerline of the billet, we will often consider the position (height z) of iso-g_s lines corresponding to a given volume fraction of solid or to a given temperature. For that purpose, we introduce the

Table IX. Rheological Parameters for AA5182 Alloy at Moderate Temperature (T is the Temperature Expressed in Kelvin)

$\kappa = c_1^\kappa + c_2^\kappa T + c_3^\kappa T^2 + c_4^\kappa T^3 + c_5^\kappa T^4$				
c_1^κ	c_2^κ	c_3^κ	c_4^κ	c_5^κ
-2.555×10^8	5.805×10^6	-1.96×10^4	25.934	-1.2×10^{-2}
$\eta = c_1^\eta + c_2^\eta T + c_3^\eta T^2 + c_4^\eta T^3 + c_5^\eta T^4$				
c_1^η	c_2^η	c_3^η	c_4^η	c_5^η
-8.932	9.11×10^{-2}	-3.339×10^{-4}	5.361×10^{-7}	-3.2×10^{-10}
$\lambda = c_1^\lambda + c_2^\lambda T + c_3^\lambda T^2 + c_4^\lambda T^3 + c_5^\lambda T^4$				
c_1^λ	c_2^λ	c_3^λ	c_4^λ	c_5^λ
25.82	1.6894×10^{-1}	4.065×10^{-4}	-4.27×10^{-9}	-4.37×10^{-12}

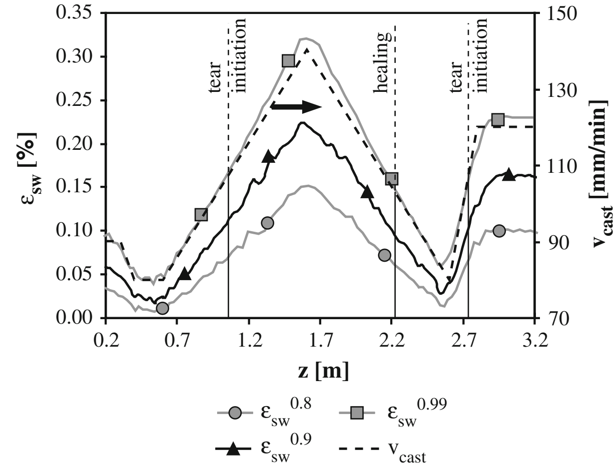

Fig. 13—Volumetric strain cumulated up to a given solid fraction plotted against the position of the isotherm corresponding to the same solid fraction along the centerline of the billet.

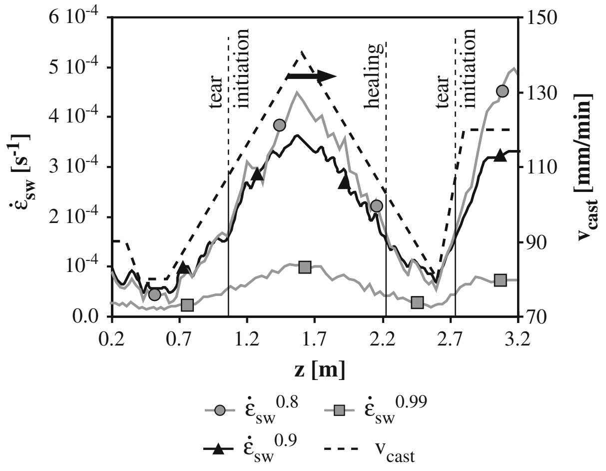

Fig. 14—Swelling strain rate evaluated at a given solid fraction, as a function of the position along the centerline of the isotherm corresponding to the same solid fraction.

corresponding notations z^{gs}, *e.g.*, $z^{0.75}$, to denote the position $r = 0$ and height $z(g_s = 0.75)$, and z^T, *e.g.*, z^{570}, for the position $r = 0$ and $z(T = 570\ °\mathrm{C})$. This convention is illustrated in Figure 11. Before discussing in detail the simulation results, it is necessary to note that the validity of the thermal model was found to be satisfactory, because measurements of the sump depth were in good agreement with the simulated values. Please note that, due to thermal diffusion, the maximum sump depth does not occur at the time the casting speed is maximum: it is delayed by approximately 140 mm, according to the measurements, and by 130 mm in the simulations.[18]

The first mechanical result we shall consider is the amount of volumetric strain cumulated up to some volume fraction of the solid g_s and noted $\varepsilon_{sw}^{g_s}$. This result can be plotted against the corresponding z^{gs} position (Figure 13). As expected, the cumulated strain increases with both the volume fraction of solid g_s and the casting speed v_{cast}. As a consequence, this cumulated volumetric strain is high in regions in which hot tears are found; this is the reason it may potentially be used as a hot tearing criterion. However, it is not possible to find a clearly defined value of $\varepsilon_{sw}^{g_s}$ above which hot tearing would occur. The interpretation of this result is difficult, due to the fact that the time (or the solid fraction) at which hot tearing occurred is unknown. Please note that stresses at the centerline of the billet are tensile and are higher in regions in which tearing was found. However, for the same reasons as those outlined earlier concerning strain, stress does not seem to be the best possible hot tearing tendency indicator for this case.

Along similar lines, we can consider the volumetric strain rate experienced by the alloy at some solid fraction, $\dot{\varepsilon}_{sw}^{g_s}$, as a function of the corresponding position z^{gs}. Such a result is shown in Figure 14. It is interesting to note that the strain rate does not depend very much upon g_s when $0.8 < g_s < 0.9$ (curves with circle and triangle symbols). The value of the strain rate experienced by the mushy alloy when its solid fraction is 90 pct thus appears to be an indicator relevant for study. Careful examination of the results shown in Figure 14 does, indeed, indicate that the strain rate curve for $g_s = 0.9$ has a nearly constant value at the two positions of tear initiation and at the position of tear healing. Therefore, the present results (concerning the tearing pattern) could have been predicted by considering a hot tearing criterion based on a critical strain rate $\dot{\varepsilon}_{sw}^{\mathrm{crit}} = 1.6 \cdot 10^{-4}\ \mathrm{s}^{-1}$: below this value, the centerline region is free of hot tears and above it, it is torn. We can compute $\dot{\varepsilon}_{sw}$ deep in the mushy zone and compare it to $\dot{\varepsilon}_{sw}^{\mathrm{crit}}$, to understand whether a hot tear is locally present in the billet. What cannot be predicted *a priori* at this stage using continuum-scale modeling is the actual value of $\dot{\varepsilon}_{sw}^{\mathrm{crit}}$.

Finally, please note that the amount of microporosity also varies along the centerline of the billet and increases with the casting speed. The variation in this quantity remains very small and, thus, does not appear to be a reasonable hot tearing criterion. However, it is interesting to remark that the pressure drop (in the last remaining liquid) computed by the porosity model typically varies between 12 and 20 kPa along the centerline of the billet. Using such values, together with the results from the Rappaz–Drezet–Gremaud (RDG) criterion developments, indicates that the order of magnitude of $\dot{\varepsilon}_{sw}^{\mathrm{crit}}$ is reasonably close to the value obtained in this study, by comparing numerical and experimental data (nucleation of a tear induced under a critical strain rate thus appears to be a reasonable tearing mechanism, in this case).

V. DISCUSSION

In the application of continuum-scale modeling for the prediction of hot tearing in aluminum alloys, it is necessary to keep in mind that there are some key differences between a tearing test conducted in a laboratory and an actual DC casting performed in a casthouse.

In the rig test, the thermal field is rather simple and isotherms are nearly parallel to the crack, *i.e.*, perpendicular to the tensile axis. Moreover, the mechanical conditions are well defined and controlled, because a displacement is imposed at the boundaries of the sample. In such a system, once a hot tear nucleates, it propagates through the sample until complete failure. This failure process is fast and easy to observe. As a consequence, it is possible to measure accurately the point at which hot tearing occurs in the sample and, thus, to evaluate the solid fraction of the material at the location and time at which failure occurs.

The case of DC casting is quite different. Although a quasisteady state can be considered, the thermomechanical conditions are much more complex. First, it is the temperature field, *via* thermal contraction, that controls the amount of strain experienced by the mushy alloy. Second, in the case of centerline tearing, the cracks are perpendicular to the isotherms, *i.e.*, the tensile stresses are perpendicular to the thermal gradient. Third, local failure may occur without the entire billet being rapidly broken. These factors contribute to the fact that it is not possible to know precisely what the solid fraction of the mushy alloy is at the location and time of failure. Finally, it is interesting to remark that the hot tear may extend through the entire billet, if the crack tip is simply able to follow the traveling mushy zone. Such a propagation mechanism (growth of the tear due to translation of the weak region of the material) is quite different from the typical nucleation and growth of a crack, as obtained in a more standard tensile test.

Having considered these aspects, it is not surprising that different hot tearing criteria might have to be applied under different circumstances. In the case of the tensile test, the present study indicates that the results can find a better explanation if a critical strain above which the mushy alloy fails is considered. It has been shown that the ductility (strain at failure, as shown in Figure 9) depends primarily on the solid fraction and only weakly on the strain rate. For the DC-cast billet, an approach based on a critical cumulated strain can also be attempted for the prediction of hot tearing. However, this prediction is more accurate if one considers a critical strain rate above which hot tears form. Such a criterion is equivalent to the RDG approach,[4] which is known to be very efficient in DC casting situations.[29] The RDG criterion does, indeed, consider a strain rate that is perpendicular to the thermal gradient. This situation is actually encountered in actual DC casting experiments, but not in tensile tests such as the one investigated here. It is thus not surprising to find that the RDG criterion may be a good hot tearing criterion for DC casting but not for the tensile testing of mushy alloys. These observations lead to the conclusion that it is probably too simple to consider a single criterion for the prediction of hot tearing under various conditions.

The present approach illustrates how continuum-scale modeling can be used in the context of hot tearing. It is, indeed, possible to take into account the entire scale of the actual solidification process. Various indicators can be calculated on length scales that range from meters down to millimeters. Such data are very useful, because it provides an accurate description of what the mushy alloy experiences locally (in terms of strain state, temperature, *etc*.). However, the limits of this "process-to-defect" approach also appear in this work. For example, combining detailed models and experimental data, it is, indeed, possible to show that strain-rate-based criteria are probably the most suited for the prediction of hot tearing in DC casting conditions. However, what is lacking in this modeling approach is the prediction of the critical value of the strain or strain rate that the alloy can withstand without failing. This information would, indeed, allow prediction of the location at which the hot tear will be found (as opposed to the present criterion approach, which can only indicate the location at which the probability of finding a tear is maximum).

It thus seems obvious that the present model will become even more useful when coupled to a granular approach such as that developed by Vernède *et al*.[30] The latter technique is based upon a "microstructure-to-defect" philosophy and covers length scales that range from tens of microns to centimeters. In such a multiscale/multiphysics approach, the local temperature, strain rate, *etc*., would be computed using the continuum approach at the scale of the casting. These values could then be used as boundary conditions for a much more local granular simulation performed for a critical region of the mushy zone at which tears are expected.

VI. CONCLUSIONS

In this article, the application of a process-scale, two-phase modeling approach is detailed in the context of both a tensile test performed under laboratory conditions and the DC casting of a billet under realistic industrial conditions. For these cases, the simulation approach could be validated satisfactorily against experimental data. Moreover, the modeling results could be used to gain further insight into the hot tearing phenomenon in these situations. This study indicates that the conditions and mechanisms involved in hot tearing may be quite different from one case to another. As a consequence, the most relevant way of predicting this failure mode also varies: cumulated strain-based criteria seem more suited for tensile test situations, while the case of the billet is better described using a strain-rate-based criterion. Moreover, this study illustrates what can and cannot be done for hot tearing predictions using a continuum-scale modeling approach. It seems clear that the next step toward fully predictive hot tearing calculations would involve coupling between accurate two-phase models, such as the one presented here, and granular models. The latter approach would allow obtaining a deeper understanding of both the different failure modes involved in hot tearing and the critical values of the hot tearing indicator best suited to a given situation.

ACKNOWLEDGMENTS

This work was carried out as part of the POST project. The authors acknowledge the Commission for Technology and Innovation (CTI, Grant No. 6167.1) and the industrial partners (Alcan (Switzerland and France)), HydroAluminium (Germany), Umicore (Brussels, Belgium), and General Motors (Detroit, MI) are acknowledged for their financial support. Finally, the authors thank Drs. G. Couturier, J.-M. Drezet, and O. Ludwig for their help with the porosity module and mechanical models; the authors also thank J.-L. Desbiolles for his assistance with aspects of the software.

REFERENCES

1. D.G. Eskin, Suyitno, and L. Katgerman: *Prog. Mater. Sci.,* 2004, vol. 49, pp. 629–711.
2. U. Feurer: *Giessereiforschung*, 1976, vol. 28, pp. 750–80.
3. T.W. Clyne and G.J. Davies: *J. Brit. Foundry*, 1981, vol. 74, pp. 65–73.
4. M. Rappaz, J.-M. Drezet, and M. Gremaud: *Metall. Mater. Trans. A*, 1999, vol. 30A, pp. 449–55.
5. D. Warrington and D.G. McCartney: *Cast Met.*, 1989, vol. 2, pp. 134–43.
6. J.A. Spittle and A.A. Cushway: *Met. Technol.*, 1983, vol. 10, pp. 6–13.
7. J.-M. Drezet and M. Rappaz: *Metall. Mater. Trans. A*, 1996, vol. 27A, pp. 3214–25.
8. M. M'Hamdi, A. Mo, and H.G. Fjaer: *Metall. Mater. Trans. A*, 2006, vol. 37A, pp. 3069–83.
9. O. Ludwig, J.-M. Drezet, C.L. Martin, and M. Suéry: *Metall. Mater. Trans. A*, 2005, vol. 36A, pp. 1525–35.
10. C. Pequet, M. Gremaud, and M. Rappaz: *Metall. Mater. Trans. A*, 2002, vol. 33A, pp. 2095–2106.
11. D.J. Lahaie and M. Bouchard: *Metall. Mater. Trans. B*, 2001, vol. 32B, pp. 697–705.
12. B. Magnin, L. Maenner, L. Katgerman, and S. Engler: *Mater. Sci. Forum*, 1996, vols. 217–222, pp. 1209–14.
13. V. Mathier, M. Rappaz, and A. Jacot: *Model. Simul. Mater. Sci. Eng.*, 2004, vol. 12, pp. 479–90.
14. S. Vernède and M. Rappaz: *Philos. Mag.*, 2006, vol. 86, pp. 3779–94.
15. A. Stangeland, A. Mo, M. M'Hamdi, D. Viano, and C. Davidson: *Metall. Mater. Trans. A*, 2006, vol. 37A, pp. 705–14.
16. M. M'Hamdi, S. Benum, D. Mortensen, H.G. Fjaer, and J.-M. Drezet: *Metall. Mater. Trans. A*, 2003, vol. 34A, pp. 1941–52.
17. V. Mathier, J.-M. Drezet, and M. Rappaz: *Model. Simul. Mater. Sci. Eng.*, 2007, vol. 15, pp. 121–34.
18. V. Mathier: Doctoral Thesis, Ecole Polytechnique Fédérale de Lausanne, Lausanne, Switzerland, 2007.
19. V. Mathier, P.-D. Grasso, and M. Rappaz: *Metall. Mater. Trans. A*, 2008, vol. 39A, pp. 1399–1409.
20. V. Mathier, J.-M. Drezet, and M. Rappaz: MCWASP XI, Opio, France, The Minerals, Metals & Materials Society, TMS, Warrendale, 2006, pp. 643–50.
21. O. Ludwig, J.-M. Drezet, P. Ménès, C.L. Martin, and M. Suéry: *Mater. Sci. Eng. A*, 2005, vols. 413–414, pp. 174–79.
22. W.M. Van Haaften, B. Magnin, W.H. Kool, and L. Katgerman: *Metall. Mater. Trans. A*, 2002, vol. 33A, pp. 1971–80.
23. H.G. Fjaer and A. Mo: *Metall. Trans. B*, 1990, vol. 21B, pp. 1049–61.
24. L.C. Nicolli, A. Mo, and M. M'Hamdi: *Metall. Mater. Trans. A*, 2005, vol. 36A, pp. 433–42.
25. B. Commet, P. Delaire, J. Rabenberg, and J. Storm: *Light Met.*, 2003, pp. 711–17.
26. P.-D. Grasso: Doctoral Thesis, Ecole Polytechnique Fédérale de Lausanne, Lausanne, Switzerland, 2004.
27. J.-M. Drezet: Doctoral Thesis, Ecole Polytechnique Federale de Lausanne, Lausanne, Switzerland, 1996.
28. A. Stangeland, A. Mo, and D. Eskin: *Metall. Mater. Trans. A*, 2006, vol. 37A, pp. 2219–29.
29. Suyitno, W.H. Kool, and L. Katgerman: *Metall. Mater. Trans. A*, 2005, vol. 36A, pp. 1537–46.
30. S. Vernède, P. Jarry, and M. Rappaz: *Acta Mater.*, 2006, vol. 54, pp. 4023–34.